LAWRENCE
LIVERMORE
NATIONAL
LABORATORY

LLNL-JRNL-434073

Direct Curvature Correction for Non-Contact Imaging Modalities- Applied to Multi-Spectral Imaging

J. M. Kainerstorfer, F. Amyot, M. Ehler, M. Hassan, S. G. Demos, V. Chernomordik, C. K. Hitzenberger, A. H. Gandjbakhche, J. D. Riley

June 3, 2010

Journal of Biomediacl Optics

Disclaimer

Direct Curvature Correction for Non-Contact Imaging Modalities – Applied to Multi-Spectral Imaging

Jana M. Kainerstorfer[1, 2,*], Franck Amyot[3], Martin Ehler[4], Moinuddin Hassan[1], Stavros G. Demos[5], Victor Chernomordik[1], Christoph K. Hitzenberger[2], Amir H. Gandjbakhche[1] and Jason D. Riley[1]

1) National Institutes of Health, Eunice Kennedy Shriver National Institute of Child Health and Human Development, PPITS/SAFB, Bethesda, MD, 20892

2) Medical University of Vienna, Center for Medical Physics and Biomedical Engineering, Waehringer Str. 13, 1090 Vienna, Austria

3) National Institutes of Health, National Institutes of Neurological Disorders and Stroke, Clinical Neuroscience Program, Bethesda, MD, 20892

4) National Institutes of Health, Eunice Kennedy Shriver National Institute of Child Health and Human Development, Program in Physical Biology LIMB-SMB, Bethesda, MD, 20892

5) Lawrence Livermore National Laboratory, Livermore, CA, 94551

* To whom all correspondence should be addressed

Jana Kainerstorfer
NIH/NICHD/PPITS/SAFB
9 Memorial Drive, Room B1E11
Bethesda, MD, 20982
301-594-0352; Fax: 301-480-2427
kainersj@mail.nih.gov

Keywords: curvature correction; non-contact imaging; multi-spectral imaging; tissue oxygenation; CCD camera

ABSTRACT

Non-contact optical imaging of curved objects may result in strong artifacts due to the object's shape, leading to curvature biased intensity distributions. This artifact can mask variations due to the object's optical properties and makes reconstruction of optical/physiological properties difficult. In this work we demonstrate a curvature correction method, which removes this artifact, and recovers the underlying data, without the necessity of measuring the object's shape. This method is applicable to many optical imaging modalities, which suffer from shape based intensity biases. By separating the spatially varying data (e.g. physiological changes) from the background signal (DC component), we show that the curvature can be extracted by either averaging or fitting the rows and columns of the images. Numerical simulations showed that our method is equivalent to directly removing the curvature, when the object's shape is known, and accurately recovers the underlying data. Experiments on phantoms validated the numerical results and showed that for a given image with 16.5% error due to curvature, the method reduces that error to 1.2%. Finally, diffuse multi-spectral images were acquired on forearms *in vivo*. We demonstrated the enhancement in image quality on intensity images and consequently on reconstruction results of blood volume and oxygenation distributions.

1. INTRODUCTION

Over recent years, the unique potential of optical imaging for disease diagnostics and treatment monitoring has become evident. This has resulted in the rapid development of different optical modalities for biomedical imaging. Some of these techniques have been already moved from bench to bedside. Besides the non-ionizing nature of optical methods and their relatively cheap implementation, an attractive feature of optical imaging is that it is usually minimally invasive, often being realized as a non-contact imaging technology, e.g., near-infrared fluorescence imaging (1), colorimetry (2, 3), tissue reflectance spectroscopy (4), polarization imaging (5-7), Pearson correlation imaging (8-10), and diffuse multi-spectral imaging (11-16). Though more convenient or even practical for many clinical applications, non-contact imaging can become a quantitative technique, only if data processing adequately takes into account the shape of the target object (e.g., body surface). The bias, introduced into optical images by the surface curvature of the object, can mask real distributions of optical characteristics of the media which characterize physiological status of the region of interest, making even qualitative assessment impossible without specially developed methods to remove curvature related image artifacts. An example of the curvature effect can be seen in Figure 1a and 1b, where we see the distortion of the images due to curvature. The images were acquired by diffuse reflectance imaging at a wavelength of 800nm and respectively show a volunteer's forearm and a cylindrical phantom. For comparison, Figure 1c shows an image of a flat phantom with the same optical properties as the cylindrical one, but no curvature.

When trying to remove the effect of curvature on reflected intensity, two general approaches are possible. Either the object's shape is being measured and taken into account or the curvature effect, which is the intensity bias, is being extracted. Several methods aimed at curvature artifact correction have been discussed recently in the literature. These approaches include hardware modification, changes in the measurement protocol and image processing techniques to qualitatively reduce the curvature effect. All these approaches have in common that the shape is being extracted rather than the effect of shape. Westhauser et al (17) illuminated the object with fringe patterns and acquire data from three cameras for extracting the surface curvature. Another approach is to use structured light generated by a beam splitter mounted on a laser diode and reconstructing the surface by an optical triangulation approach (18, 19). However, these approaches require hardware modification and additional measurements to extract the shape of the object before extracting and removing the intensity artifacts. Gioux et al (20) combined phase-shifting profilometry for shape extraction and modulated imaging for optical properties measurements into one single instrument. The same group showed that modulated imaging is a powerful tool for reconstruction of absorption and scattering coefficient and that low spatial frequencies are maximally sensitive to absorption contrast (21). The combination of these approaches into one machine does therefore not require any hardware modification, but still additional measurements. Another approach was developed by Zeman et al., which is based on image processing and which is used for non-quantitative image enhancement (22). This is not a correction model, however, and is not useful for quantitative modeling as it cannot provide real intensity values. At this

time, no techniques, to our knowledge, have been proposed for quantitative curvature extraction and removal in the images which do not involve additional measurements.

In this paper we are introducing a correction method, which extracts and corrects the curvature intensity bias, rather than measuring the shape of the object. It is not dependent on the imaging modality and does not require any additional measurement on the object. To demonstrate and evaluate the method, we are considering the case of diffuse multi-spectral imaging, which measures the diffuse reflection from the skin, using a flat light illumination. Spatial frequencies in the data are therefore not sensitive to absorption contrast. This technique is used to reconstruct and map blood volume and blood oxygenation concentrations. The acquired images are often biased by the curvature of the objects (11-16). This problem has to be addressed after acquisition of the images because clinical protocols typically prohibit patient skin manipulation to flatten the skin surface for curvature removal.

The method we are proposing for extracting and correcting the curvature effect is computationally inexpensive, adding only a few seconds to the analysis, and robust, as we will be demonstrating in the results section. It is based on the diffuse reflectance images acquired and does not require additional measures of the objects shape. As it is based on intensity images, it can be applied to any imaging modality, which captures diffuse reflectance images. In our approach, the curvature effect can be removed from existing data, by either averaging or fitting of the intensity images, without direct shape reconstruction. Our goal is to separate the effects of curvature and skin chromophore variations in the images. We demonstrate that the curvature effect can be separated by either averaging or fitting the rows and columns of the image, giving access to the

chromophore dependent variation. Limitations of the method lay in the object's shape when using the averaging approach and in the choice of fitting function used for the fitting approach. The advantage of this suggested method is not only that no additional measures are necessary, but also that previously collected data can be re-analyzed to remove curvature effects.

In order to demonstrate the strengths and limitations of the method we applied it to numerically simulated objects, phantoms, and in vivo data. We would like to point out that the cases presented here are examples for demonstrating the performance of the algorithms, which might differ for different objects imaged. For the interested reader and for trying the method on images of different geometry than described here, the Matlab codes can be obtained from the corresponding author.

In the first part of the paper, we show the application of curvature correction in the case of numerically simulated objects. In the second part, we describe phantom experiments performed on cylindrical and flat objects to validate the technique experimentally. Finally, the fitting method is applied using *in vivo* acquired multi-spectral images. We demonstrate the enhancement in image quality on raw intensity images and consequently on reconstruction results of blood volume and oxygenation distributions.

2. MATERIALS

2.1. Instrumentation

A non-invasive, non-contact diffuse reflectance multi-spectral imaging system was developed in cooperation with Lawrence Livermore National Laboratory (15, 16). Polarized light from a white light source (halogen 150W, Techniquip, Pleasanton, CA) is used for flat illumination of the sample imaged. A second polarizer (Optarius, UK) is placed before the detection unit, perpendicular to the incident beam polarization, thus guaranteeing diffuse reflectance measurements and removal of specular reflection (6).

The distance (h) between the sample and detection unit was held constant ($h=500mm$), by using two He-Ne lasers at a fixed angle. The highest point of the sample was placed at the point where the two lasers intersect.

Light is then captured in a CCD camera (Princeton Instruments CCD-612-TKB, Roper Scientific) after passing consecutively one of six narrow bandpass filters (40nm FWHM, FS40-NIR-I, CVI Laser, Albuquerque, NM) on a filter wheel. Six wavelength images are taken, the wavelengths being 700, 750, 800, 850, 900 and 1000nm. Only the first four wavelengths were used for further analysis in order to avoid water and lipid absorption.

For calibration purposes, images from a 90% reflectance paper (Kodak) are taken. The raw wavelength intensity images are being divided by the normalized intensity distribution from the paper in order to remove spatial inhomogeneity from the illumination. Spectral inhomogeneity from the source is being corrected for by utilizing the spectral ratio of the six wavelengths images of the paper and thus acquiring correction

factors (15). These corrected images are then used for further processing and will be referred to as 'raw' intensity images.

2.2. Reconstruction of blood volume and oxygenation

In vivo data acquired from healthy volunteers' forearms using diffuse multi-spectral imaging was used for reconstruction of blood volume and oxygenation. Reconstruction was performed in MATLAB (Math Works, Natick, MA) by least squares non linear fitting of the data to our analytical skin model (15). Four wavelength (λ) images were used for reconstruction, being 700, 750, 800, and 850nm. The analytical skin model used is based on a two layered structure, the first one being the melanin containing epidermis, the second one being the blood containing dermis. Optical properties of the skin were taken from literature values (23-25) and are summarized in table 1. Our model is given as:

$$I_e(x,y,\lambda) = S \cdot A_e(x,y,\lambda)^2 \cdot A_d(x,y,\lambda) \qquad [1]$$

The attenuation by the epidermis, A_e, is based on Lambert's law and can be written as:

$$A_e(\lambda) = e^{-\mu_e \cdot d_e} = e^{-\left(v_m \cdot 0.66 \cdot 10^{11} \cdot \lambda^{-3.33} \cdot d_e\right)}, \qquad [2]$$

where v_m is the concentration of melanin, d_e is the thickness of the epidermis and μ_e is the absorption coefficient of the epidermis, which is based on the absorption of melanin. The attenuation by the dermis, A_d, which includes the absorption due to blood volume and oxygenation, is based on the analytical solution of photon migration in turbid media based on random walk theory (26) and can be written as:

$$A_d(\lambda) = \frac{e^{-2(\mu_d/\mu_s)}}{\sqrt{24(\mu_d/\mu_s)}} \cdot \left(1 - e^{-\sqrt{24(\mu_d/\mu_s)}}\right) \approx 1 \quad . \quad 0 \quad 6 \cdot 1(\mu_d/\mu_s)^{0.35}, \qquad [3]$$

where μ_s is the reduced scattering coefficient and μ_d is the absorption coefficient of the dermis, defined as:

$$\mu_d = v_{db} \cdot \left[(1 - v_{boxy}) \cdot \mu_{deoxy} + (v_{boxy}) \cdot \mu_{oxy}\right] \qquad [4]$$

The scaling factor *S*, blood volume, v_{db}, and blood oxygenation, v_{boxy}, are unknown a priori and were solved for.

3. METHODS

In this section, we explain in detail our curvature correction method which uses either averaging of intensity images or fitting of intensity images. Potentially each of these algorithms can be applied. However, depending on the nature of the acquired images, one may provide more accurate results than the other. After this we describe the specific model of skin chromophores incorporated into our diffuse multi-spectral imaging system. This system provides a good example for using the curvature correction because it acquires diffuse reflectance images in a non-contact fashion of objects where the curvature effects are expected to be considerable.

3.1. Curvature Correction

Our curvature correction algorithm, is based on extracting the curvature effect on intensity images, and does not require additional measures of the shape of the object. It is applicable when the curvature effect is stronger than signals due to intrinsic changes. If the curvature of the object causes intensity variations, which are smaller than intrinsic changes, the curvature effect may be considered negligible. From now on, we will refer to these changes as physiological changes, e.g. due to hematological variation. One may consider physiological changes on top of curvature as variations on top of a carrier frequency, much like AM radio signal. Extracting the curvature is similar to removal of the carrier frequency, which makes the signal (physiologically significant information) available.

The raw detected intensity $I_r(x,y)$, which is the intensity after correcting for spatial and spectral in-homogeneities of illumination, at image pixel position

$(x,y) \in \{1,...,n\} \times \{1,...,m\}$, where n and m are the total number of pixels in the horizontal and vertical image axis respectively, can be described as a function of emitted intensity ($I_e(x,y)$) from the sample surface, the distance of the detector from the object's surface ($h(x,y)$) and the angle between the surface normal of the object and the direction to the detector ($\theta(x,y)$). Assuming Lambertian reflection, we can write this dependence as

$$I_r(x,y) = C(x,y) \cdot I_e(x,y), \qquad [5]$$

where $C(x,y) = \cos(\theta(x,y))/h^2(x,y)$ is the curvature term. The assumption of diffuse reflection is valid for our multi-spectral imaging system, as the cross polarizer used removes specular reflection.

Given a separate measure of the surface, one can eliminate the curvature effect directly using this equation. In the absence of such measures, we may extract the curvature by considering it as an intensity effect. To do this, we must first recast Equation [5], separating the background intensity, I_b (DC component of the signal, constant), and information intensity, $I_d(x,y)$ (physiologically significant information, spatially varying). This gives us

$$I_r(x,y) = C(x,y) \cdot (I_b + I_d(x,y)), \qquad [6]$$

where the background I_b is independent of x and y. It will turn out that if we assume that the physiological signal $I_d(x,y)$ is much weaker than the background I_b ($I_d(x,y) << I_b$), where the magnitude of I_b is in the order of the average image intensity, we can extract and eliminate the curvature effect C(x,y). If this assumption is violated, then the method may perform poorly. We will demonstrate in the results section that the assumption $I_d(x,y) << I_b$ is valid for our physiological data.

If we further assume that the distance *h(x,y)* between the camera and the sample is much bigger than the elevation changes of the sample's surface that is due to the curvature, then *h*'s dependency on x and y is negligible. In the following we treat *h* as a constant height component that we put into I_b and I_d such that the curvature term becomes only angle dependent. We can then recast equation [6]:

$$I_r(x,y) = C'(x,y) \cdot (I'_b + I'_d(x,y)), \qquad [7]$$

where $C'(x,y)=cos(\theta(x,y))$, $I'_b=I_b/h^2$, and $I'_d(x,y)=I_d(x,y)/h^2$, with I'_b and I'_d being the background and data signal at height *h*, which is the smallest distance between the surface and camera (highest point of the sample). If the measurement is being focused on this point, *h* corresponds to the focal distance. We developed two different and independent algorithms to extract $C'(x,y)$. The use of one or the other depends on the geometry of the imaged object.

3.1.1. Known Parametric geometries

For our first method we assume that the curvature term C' only changes along the x and y axis, i.e., there are two functions C_1 and C_2, that do not have to be further specified, such that

$$C'(x,y) \approx C_1(x) \cdot C_2(y). \qquad [8]$$

For instance, this assumption holds if the object is cylindrical and aligned to either the *x* or *y* axis in the image. This applies to any geometry which can be described in a separable two part parametric function. We note, however that this requires knowledge of the underlying geometry, for example in an elliptical geometry we would need to know it's center.

The second assumption, that was already mentioned, is that the physiological signal is weak compared to the background, i.e.,

$$I_d(x,y) << I_b. \qquad [9]$$

Moreover we suppose that there is a point (x_0,y_0) on the surface whose tangent is perpendicular to the image axis. This yields $\theta(x_0,y_0)=0$ and hence

$$\max_{\substack{x=1,..,n \\ y=1,...,m}} (C'(x,y)) = 1. \qquad [10]$$

This last assumption will be satisfied for almost any geometry of objects imaged.

First, we compute the averages $r_1(y)$ and $r_2(x)$ of each column and row of I_r, respectively, i.e.,

$$r_1(y) := \frac{1}{n}\sum_{x=1}^{n} I_r(x,y), \qquad r_2(x) = \frac{1}{m}\sum_{y=1}^{m} I_r(x,y).$$

We will verify in the following that - under the above assumptions - the term

$$E(x,y) := \frac{r_1(y)\cdot r_2(x)}{\max_{y=1,..,m}(r_1(y))\cdot \max_{x=1,..,n}(r_2(x))} \qquad [11]$$

approximates the curvature term $C'(x,y)$.

To derive $E(x,y) \approx C'(x,y)$, we first try to estimate the denominator of E. The maximum of r_1 is

$$\max_{y=1,..,m}(r_1(y)) = \max_{y=1,..,m}\left(\frac{1}{n}\sum_{x=1}^{n} C'(x,y)I'_b + \frac{1}{n}\sum_{x=1}^{n} C'(x,y)I'_d(x,y)\right). \qquad [12]$$

By using $0 \le C'(x,y) \le 1$ and $I'_d(x,y) << I'_b$, the term $\frac{1}{n}\sum_{x=1}^{n} C'(x,y)I'_d(x,y)$ is negligible in [12], and we can estimate $\max_{y=1,..,m}(r_1(y)) \approx I'_b \cdot \max_{y=1,..,m}\left(\frac{1}{n}\sum_{x=1}^{n} C'(x,y)\right)$. Due to [8], this finally yields

$$\max_{y=1,..,m}(r_1(y)) \approx I'_b \cdot \frac{1}{n}\sum_{x=1}^{n} C_1(x) \cdot \max_{y=1,..,m}(C_2(y)). \qquad [13]$$

Analogously, we obtain

$$\max_{x=1,..,n}(r_2(x)) \approx I'_b \cdot \frac{1}{m}\sum_{y=1}^{m} C_2(y) \cdot \max_{x=1,..,n}(C_1(x)). \qquad [14]$$

Due to [8] and [10], we have $1 = \max_{\substack{x=1,..,n \\ y=1,..,m}}(C'(x,y)) \approx \max_{y=1,..,m}(C_1(y)) \cdot \max_{x=1,..,n}(C_2(x))$, and [13] and [14] then yields that the denominator of $E(x,y)$ is approximately given by

$$I'_b \cdot I'_b \cdot \frac{1}{n}\sum_{x=1}^{n} C_1(x) \cdot \frac{1}{m}\sum_{y=1}^{m} C_2(y). \qquad [15]$$

The numerator

$$r_1(y) \cdot r_2(x) = \frac{1}{n}\sum_{x'=1}^{n}(C'(x',y) \cdot (I'_b + I'_d(x',y))) \cdot \frac{1}{m}\sum_{y'=1}^{m}(C'(x,y') \cdot (I'_b + I'_d(x,y')))$$

can be expanded such that

$$r_1(y) \cdot r_2(x) = \frac{1}{n} \cdot \frac{1}{m}\sum_{\substack{x'=1 \\ y'=1}}^{n,m} C'(x',y) \cdot I'_b \cdot C'(x,y') \cdot I'_b + T(x,y),$$

where T captures the missing terms. The assumption [9] implies $\frac{I'_d(x,y)}{I'_b} = \frac{I_d(x,y)}{I_b} \approx 0$ which yields $\frac{T(x,y)}{I'_b I'_b} \approx 0$. This leads to

$$\frac{r_1(y) \cdot r_2(x)}{I'_b \cdot I'_b} \approx \frac{1}{n} \cdot \frac{1}{m}\sum_{\substack{x'=1 \\ y'=1}}^{n,m} C'(x',y) \cdot C'(x,y') \approx \frac{1}{n} \cdot \frac{1}{m}\sum_{\substack{x'=1 \\ y'=1}}^{n,m} C_1(x') \cdot C_2(y) \cdot C_1(x) \cdot C_2(y'),$$

where we have used [4]. By combining this with [7] and [11], we obtain

$$E(x,y) \approx \frac{C_1(x) \cdot C_2(y) \cdot \frac{1}{n}\sum_{x=1}^{n} C_1(x) \cdot \frac{1}{m}\sum_{y=1}^{m} C_2(y)}{\frac{1}{n}\sum_{x=1}^{n} C_1(x) \cdot \frac{1}{m}\sum_{y=1}^{m} C_2(y)} = C_1(x) \cdot C_2(y) \approx C'(x,y). \qquad [16]$$

We can now divide I_r by E which gives us the desired

$$\frac{I_r(x,y)}{E(x,y)} \approx I'_b + I'_d(x,y). \qquad [17]$$

The retrieved intensity $I'_e = I'_b + I'_d$ is the emitted intensity at the focal distance *h*. If different distances are used for multiple samples, one must further calibrate for the h^2 component of *C(x,y)*.

A drawback of the above approach is its limitation to curvature terms $C'(x,y) \approx C_1(x) \cdot C_2(y)$. This condition is violated as soon as the sample has an unknown / complex geometry.

3.1.2. Generalized geometries

To circumvent the limitation of having a known geometry, we have developed a second numerical method that is based on iterative polynomial fitting of the intensity image. We skip assumption [8], but we keep [9] and [10]. Removal of the data signal $I'_d(x,y)$ to retrieve $C'(x,y) \cdot I'_b$ is done by local smoothing. A polynomial function is fitted for each row and each column in the image I_r using the polyfit function in MATLAB (Math Works, Natick, MA).

The polynomial function is fitted for each row ,

$$p_x(y) = p_{x,\alpha} y^{\alpha} + p_{x,\alpha-1} y^{\alpha-1} + ... + p_{x,1} y^1 + p_{x,0} \qquad x \in \{1,...,n\}$$

and each column

$$q_y(x) = q_{y,\beta} x^{\beta} + q_{y,\beta-1} x^{\beta-1} + ... + q_{y,1} x^1 + q_{y,0} \qquad y \in \{1,...,m\}$$

where α and β are the polynomial orders. This results in two surface fits of the image. We expect that the spatial average of these 2D fits gives the first approximation $\left[C'(x,y)\cdot I'_b\right]^1$ of the background modulated by the curvature, i.e.,

$$\left[C'(x,y)\cdot I'_b\right]^1 := \frac{p_x(y)+q_y(x)}{2}. \qquad [18]$$

The first fit of the curvature $C'(x,y)\cdot I'_b$ provides a reasonable resemblance of the object's surface, but is still an approximation. In the presence of a spatially varying data signal, the first fit of the curvature will not be smooth. Considering Equation [18] as being a function of the image,

$$\left[C'(x,y)\cdot I'_b\right]^1 = f\left(I_r\right) \qquad [19]$$

we may iterate the curvature fit, using

$$\left[C'(x,y)\cdot I'_b\right]^k := f\left(\left[C'(x,y)\cdot I'_b\right]^{k-1}\right), \qquad [20]$$

where k is the number of iterations. Performing this iterative fitting will smooth the curvature fit and eliminate distortions which might be present in the first fit.

The choice of fitting function used is based on the geometry of the object. Here we are considering a forearm and will show in the results section that a fifth order polynomial in horizontal and vertical direction fits the data best and that six iterations were sufficient for the fitting procedure. For consistency, we have used these fitting parameters for all results.

Due to [9] and [10], the maximum of I_r is essentially given by

$$\max_{\substack{x=1,\ldots,n\\ y=1,\ldots,m}} I_r(x(y,\ )\approx) I'_b \cdot \max_{\substack{x=1,\ldots,n\\ y=1,\ldots,m}} C(\ 'x(y,\ )=) I'_b .$$

By assuming that $\left[C'(x,y)\cdot I'_b\right]^k \approx C'(x,y)\cdot I'_b$, for $k=6$, we can compute

$$\frac{\left[C'(x,y)\cdot I'_b\right]^k}{\max\limits_{\substack{x=1,\ldots,n\\ y=1,\ldots,m}}\left(I_r(x,y)\right)} \approx \frac{C'(x,y)\cdot I'_b}{I'_b} = C'(x,y)\,. \qquad [21]$$

The constraint of this method lies in the choice of the fitting function used. Care must be taken that the spatial frequency of the fitting function chosen is lower than that of the signal, or in other words, that the fitting function used does not fit the data. Otherwise the fitting function used will fit and remove the data content as well. This curve fitting method was evaluated using the numerical simulation, experimental phantom, as well as *in vivo* data.

3.2. Numerical Simulation

A data wave was placed on a 50mm radius cylinder with a distance of 400mm away from the detection plane. To test the theory we used a background (or average) intensity of unit value and applied to it a sine grating signal of amplitude 1% of the background. We tested and compared three approaches, the approach where we have a measured surface (exact kernel), the averaging approach and fitting model. We used equation 6 to create the cylindrical numerical object and the exact kernel deconvolution inverts equation 6 to extract the emitted intensity, $I_e(x,y)$, with all variables known. The exact kernel is used as a gold standard to compare the averaging and curve fitting method to, and is equivalent to having a separate system to measure shape.

As no imaging technique is free of noise, we evaluated the performance of our curvature correction method in presents of noise. Noise is defined as average white Gaussian noise applied to the final signal (background plus data wave modulated onto the cylinder) with magnitude determined as a percentage of the original data wave.

3.3. Phantom Experiments

We used a cylindrical tube embedded in blue paper and flat blue paper, which will be referred to as cylindrical phantom and flat phantom, respectively. The blue paper used was regular office paper and several layers of paper were used to avoid any reflected light from the underlying tube. The diameter of the cylinder was 74mm. Structures were introduced by imprinting shaped objects (letters) on the phantoms. We used pencil, black, and red permanent markers, which will be referred to as contrast agents. Different contrast agents result into different data to background (DC component) ratios (I_d/I_b). For these experiments, optical properties of the paper and contract agents were not known and not relevant. In order to experimentally test the curvature correction approaches, the quantity to change was the ratio of data to background (I_d/I_b). In order to calculate the ratio, we imaged the flat phantom with the same letters imprinted and evaluated the data signal (I_d) and the background signal (I_b) by the following equations.

$$I_d = \frac{\max\left(I_e(x,y)\right) + \min\left(I_e(x,y)\right)}{2} \qquad [22]$$

$$I_b = \frac{\max\left(I_e(x,y)\right) + \min\left(I_e(x,y)\right)}{2} \qquad [23]$$

The ratios (I_d/I_b) for the different contrast agents at wavelength 800nm were 0.73 (black marker), 0.51 (red marker), and 0.39 (pencil).

3.4. In Vivo Experiments

Multi-spectral images were taken on healthy volunteers' forearms. All subjects signed a consent form, which was approved by the Institutional Review Board (IRB) of the National Institutes of Health under the protocol 08-CH-0001.

4. RESULTS

4.1. Numerical Simulation

In Figure 2, we show that in the case of a data wave in form of a sine grating (a), superimposed on a cylindrical shape object (created using Equation [6]), (b-i) without noise and (b-ii) with 50% noise, we can recover the data wave using any of the three considered approaches. These approaches are (c) exact kernel, (d) averaging and (e) curve fitting approach. (c-i to e-i) Show the deconvolution without noise, (c-ii to e-ii) show the deconvolution with noise. (ii) Shows that in the case of noise, all three models respond to noise in a qualitatively similar manner and allow reliable recovery of the data wave. The point-wise percentage error is shown in column (iii); it is the deconvolved data wave (ii) minus the data wave (a-i), divided by the data wave. Wherever the data wave is of zero value, the error goes to infinity (division by zero). Remarkably this shows that all three approaches perform qualitatively equivalently. In order to demonstrate that the response to noise of the three models is also quantitatively equivalent, we have taken a set of images over a noise range of 1 to 100% (data not shown). Results show that the average error is the same for all approaches over the entire noise range and stays around zero. The normalized standard deviation shows an equivalent linear trend for all three methods and goes from 0.03 at zero noise to 0.537 at 100% noise applied.

In Figure 3a, we assess the dependence of the objects alignment relative to the horizontal or vertical image axis. The cylindrical numerical object was rotated 90 degrees in 5 degree steps and the error in reconstruction caused by this rotation was calculated. As expected, the averaging approach depends on the objects orientation, whereas the curve fitting approach does not. In Figure 3b, we show the effect of varying the radius of

the cylinder, therefore the maximum angle theta, whist holding the image size constant at 50mm, on the error on reconstructed data. The angles evaluated were 25 – 85 degree. The averaging method is not influenced by changes in angle, therefore changes in the curvature, and recovers the data wave accurately in all cases. The curve fitting method shows an exponential increase in error with increasing angles. At 85 degrees the error is 0.47, which is 47 times larger than the data wave. At angles greater 85 degrees the curve fitting approach brakes down and shows a dependence on sampling accuracy. The exponential increase in error can be explained by the fact that a polynomial function cannot fit a cylinder. When excluding high angles (> 35 degree), therefore only taking a fraction of the cylinder into account, the curve fitting method performs well, with an error smaller than the data wave. For all other numerical simulation results, a radius of 50mm (30 degrees) was used where the error is much smaller than the data wave ($2.6x10^{-4}$).

In Figure 4a, we illustrate a potential limitation of the curve fitting approach. Two columns of images are shown, the left column being the target data wave and the right being the deconvolved data wave. Here we have reduced the spatial frequency (top to bottom) of our sine grating gradually towards a point where the polynomial function used for fitting begins to fit the data wave. In this degenerative case we know that the model will not hold. This is expected, but as asserted, such cases should not occur in typical biological samples, which will be demonstrated in the *in vivo* result section. In figure 4b we provide a quantitative analysis of this effect. The average error in reconstruction is plotted against the number of cycles of the sine grating in the data wave. With increasing number of cycles, or spatial frequency, the error in reconstruction for the curve fitting

method decreases. As expected, the averaging approach is not affected by the spatial frequency of the data wave.

Figure 5 shows an assessment of our fundamental assumption that $I_d << I_b$. The percentage error in reconstruction is plotted against data to background ratio. Ratios evaluated were up to 1, where the data equals the background. Physiologically reasonable ratios, assessed by the *in vivo* results, were in the order of 0.15. As expected, the error increases with increased ratio for the curve fitting method. Whilst the I_d/I_b ratio is needed for the theoretical derivation, the averaging approach appears unaffected by the I_d/I_b ratio and performs equivalently to the known geometry model.

With the numerical simulation we have shown that all three approaches of extracting the curvature are equivalent, qualitatively and quantitatively, and can accurately recover the data wave. We showed the dependence of the results on noise and assessed the potential limitations of the numerical approaches.

4.2. Phantom Experiments

Multi-spectral images were acquired from a cylindrical and a flat phantom with the same optical properties. For illustrative purposes and conciseness, images will only be shown at one wavelength (800nm). We evaluated the curve fitting approach and we will illustrate the importance of adequate choice of polynomial order for fitting, the qualitative and quantitative recovery of the object shape, as well as the limitations of the algorithm with high background to data ratio.

In Figure 6 we show the effect of polynomial order on fitting quality. An averaged cross-section along the cylinder axis after correction can be seen (a).

Polynomial orders two and three reduce the curvature effect but do not remove it completely at the edges. No significant difference can be seen between order five and six, which both remove the curvature accurately. Minor residuals (<2%) can be seen at the edges of the cylinder, which can be explained by the high angular dependence of the objects shape at the edges as well as by the fitting function used. A polynomial function cannot fit a circle and breaks down at the edges. We generated L-curves in order to make a decision of the best choice of polynomial order for fitting. The normalized standard deviation of all six wavelengths images, after correction for each polynomial order, was calculated. The standard deviation for each L curve was normalized against the maximum standard deviation for each wavelength and the dependence of standard deviation on the polynomial order can be seen in Figure 6b. Based on these L-curves we chose fifth order polynomials for the curve fitting approach for our case.

Figure 7 shows the cylindrical phantom (a) before and (b) after curvature correction with the curve fitting approach in comparison to (c) the flat phantom. We demonstrate that our algorithm is capable of removing the curvature effect qualitatively in the comparison of Figures 7b and 7c. In Figure 7d we illustrate this recovery quantitatively by showing the averaged cross section for (a-c) with error-bars given by the standard deviation over all rows. The mean intensities over the entire image area are 68105±997 and 65930±1095 for the curvature corrected and the flat phantom respectively. Values are greater than the saturation limit of the 16bit camera due to calibration for spectral inhomogeneities (15) and due to the curvature correction. Remaining discrepancies between theses numbers may be explained by the fact that we used a cylindrical phantom, which cannot be fitted perfectly by a polynomial function. In

comparison, the uncorrected phantom mean intensity is 55022±15760. We therefore show that real intensity values can be recovered within 1.2% error, which is in comparison to 16.5% error before correction

Figure 8 shows the cylindrical phantom with different contrast agents, having decreasing data to background ratios (a-c). The contrast agents used have different absorption coefficients compared to the background and were therefore used to mimic local changes, which are present for *in vivo* imaging (vein, hair, lesion, etc.). Different contrast agents were used in order to see the effect of contrast on the curvature correction. The method used for correction was based on the curve fitting approach. Letters were written perpendicular to the axis of curvature (i and ii) and along it (iii and iv) in order to assess the effect of structure orientation on the curvature correction. Figure 8a shows that for the highest I_d/I_b ratio (black marker), the least effective curvature correction is achieved. From left to right, Figure 8a shows the phantom (i) before correction and (ii) after correction for letters aligned perpendicular to the curvature, (iii) before and (iv) after correction for letters aligned along the curvature. After correction, remaining curvature is clearly visible in the image area where the letters are written, regardless of orientation. In this case the I_d/I_b ratio was 0.73 (calculated using equations 22 and 23), which is a much higher ratio than physiological changes found in typical biological samples. Qualitative improvement can be seen in Figure 8b and 8c (ratios 0.51 (red marker) and 0.39 (pencil) respectively), where the algorithm works better, as the ratio decreases.

The quantitative relationship between the I_d/I_b ratio and the normalized standard deviation of the curvature corrected image is shown in Figure 9. For this comparison, the standard deviation of the background (no letters) was calculated after correction, as it is

the background (no letters) which should be equivalent for all contrast agent images. Both cases of feature alignment were considered, perpendicular and along the curvature axis. The descending trend of standard deviation for decreasing ratios is found for both directions of feature alignment. Features which are aligned along the axis of curvature are less disruptive to the correction than features perpendicular to the curvature axis.

The phantom experiments demonstrated that our algorithm does not only qualitatively remove the curvature, but provides quantitative agreement with flat objects with the same optical properties. We investigated the influence of data to background ratio on the correction efficiency and show that if the ratio is too high, the algorithm may not remove the curvature completely.

4.3. In Vivo Experiments

We evaluated the curve fitting curvature correction method described in the previous sections using *in vivo* images taken by our multi-spectral imaging system. Specifically, using images of a healthy volunteers lower arm, we will show the improvement in intensity image quality as well as on the reconstruction results for blood volume and oxygenation.

Figure 10 shows the effect of multiple iterations on the curvature fit, when using the curve fitting approach. Figure 10a shows a cross-section through the curvature fit with veins present. The locations of veins are pointed out by black arrows. The first fit of the curvature is clearly biased by intensity variations due to veins. This effect disappears with increasing numbers of iterations and the curvature becomes smooth. To quantify this

behavior, the squared error of the difference between fits over increasing iterations was calculated, which can be assessed as:

$$E_n = \left(\left\langle C'(x,y) \cdot I_b' \right\rangle^{l-1} - \left\langle C'(x,y) \cdot I_b' \right\rangle^{l} \right)^2, \qquad [24]$$

where l: 2 → L, with L being the maximum number of iterations. The results of the squared error are shown in Figure 10b. Based on this L-curve, we have chosen six iterations for our curvature correction method.

The qualitative improvement of image quality and feature extraction on intensity images for all six wavelengths acquired can be seen in Figure 11. Our method is able to recover real intensities and therefore spectral ratios are retained, which makes further analysis, i.e. reconstruction for blood volume and oxygenation, possible. The curvature corrected images in Figure 11 were used to evaluate the data to background ratios and to confirm that our assumption of $I_d << I_b$ holds for our multi-spectral images. The data signal (I_d) and the background signal (I_b) were calculated by equations 22 and 23 using the curvature corrected images. We were confident using the corrected images for calculation, as the curvature effect is clearly larger than the data variation, as can best be seen in figure 12e and 12f (corrected vs. uncorrected). The ratios (I_d/I_b) for all six wavelengths images were calculated and were 0.12 (700nm), 0.15 (750nm), 0.16 (800nm), 0.16 (850nm), 0.13 (900nm), and 0.09 (1000nm). Comparing these ratios to the results of the numerical simulation (Figure 5), a maximum error of 1.2% is expected in the removal of the curvature effect.

To assess the improvement on skin chromophore concentration image reconstruction for blood volume and oxygenation was performed; representative results are shown in Figure 12. Reconstruction was performed on uncorrected intensity images

and the corresponding curvature corrected ones in order to evaluate the curvature effect on reconstruction of chromophore distribution and concentration. Figure 12a and 12b show the reconstruction results for uncorrected images. Almost no structures can be identified, which is even more evident when looking at a cross section through the images, indicated by the dotted line in 12a and plotted in 12e and 12f. The curvature is clearly visible in both (a) blood oxygenation and (b) blood volume maps. The effect leads to overestimation of oxygenation in the center of the image and underestimation at the edges; the opposite effect is visible for blood volume. The curvature biases the reconstruction not only towards higher or lower chromophore concentrations, but obscures the structures in the sample imaged. Figure 12c and 12d show the results for curvature corrected images. The overall distribution of chromophore concentration is more uniform and not biased by the curvature anymore. A cross sectional comparison between uncorrected and corrected images can be seen in Figure 12e and 12f. With the curvature correction applied, pixel-wise assessment of chromophore concentration and detailed assessment of small structures was made possible.

We demonstrated the qualitative improvement of curvature correction for multi-spectral images of *in vivo* data. The importance of correction becomes evident in the reconstruction results, where the curvature highly biases the spatial distribution of chromophore concentrations and makes pixel-wise assessment impossible. We further demonstrated that detailed feature extraction became possible, allowing assessment of structures over the entire image.

DISCUSSION

Direct approaches to curvature correction in non-contact imaging allow us to remove the curvature artifact without extra measurements being required. We present two approaches that may be used in a complementary fashion depending on the imaging paradigm and sample imaged. The performance of the approaches depends on the objects images and the spatial extend of the data. Examples shown here shall therefore be seen as examples.

Numerical simulations allowed us to compare the two methods to an exact kernel deconvolution. The exact kernel is equivalent to measuring the geometry precisely with a secondary instrument, as such it provides a gold standard of the best possible result. We showed that the recovered signal is qualitatively (Figure 2) and quantitatively equivalent to the exact kernel. Figure 2 illustrates the images recovered from the two methods in the presence of noise, showing qualitative agreement to the exact kernel. We showed that over a range of noise up to 100% that the error in these images is numerically matched to that of the exact kernel. From these results we can assert that the two methods perform with the same quantitative performance as a separate measurement approach. This performance is demonstrated experimentally in Figure 7, where we recover the intensity value of a curved object to within 1.2% (average over the image); the average error in the uncorrected image is 16%.

The correction of the curvature is achieved by extracting information from the original intensity image. The information is the shape dependent bias in the image as described in equation 5. We extract this information by one of two methods, the first method is to use an x/y averaging algorithm. This method gives good qualitative and

quantitative results as shown in figure 2. However it is limited by the assumption given in equation 8. This constrains us to images with simple geometries aligned to the imaging frame of reference. For the case of generalized geometries we have developed a curve fitting method as an alternative approach to extract the information. As illustrated in figure 3a, we see that the averaging method does indeed break down significantly with as little as 5% change in angular orientation to the imaging frame of reference. As expected, our generalized curve fitting model performs equivalently to the exact kernel through all orientations.

Having demonstrated the improvement of the generalized curve fitting approach over the averaging method, we now discuss the limitations of this approach where the averaging approach may prove more suited to a given curvature correction problem. The first limitation is evidenced in figure 3b, where we see under areas of high curvature the curve fitting approach does not recover the background levels as accurately as an exact kernel, however the averaging approach is unaffected in this case. The second limitation of the curve fitting approach lies in the choice of the fitting function, which has to be chosen carefully, so that it fits the curvature of the object without fitting the spatially varying data signal. The curve fitting method rapidly degenerates both qualitatively (figure 4a) and quantitatively (Figure 4b) when the spatial frequencies are low. The averaging method is again not affected by such spatial frequency constraints (Figure 4b). Examples of physiological conditions, for which the described curve fitting method is suitable for, are port wine stains, body parts similar in structure, as described here, wounds, skin lesions, and others. The latter two are suitable conditions to study, if they are large compared to the image size and thus occupy most of the image. In general, the

curve fitting method, with its parameter as chosen for this presented work, brakes down, if features in the image are of low spatial frequency. Examples of those cases could include nevi, lesions, if small compared to image size, and others. The final limitation of the curve fitting method is in the I_d/I_b ratio. Both methods require that $I_d << I_b$ and the curvature extraction rapidly degenerates as $|I_d| \rightarrow |I_b|$ (see figure 5); no such degeneration is seen for the averaging approach when using a sine grating as data wave.

For the case of Multi-Spectral imaging we wish to choose the most appropriate method. We know that these images may come from any part of the body and therefore the geometry may not be suitable to the averaging method, without rotation and image segmentation. This suggests the curve fitting approach would be more suitable, however we must first consider the other limitations. We know that the spatial variation of the chromophores is high, and that the images will not typically contain high curvature, however we must consider the ratio (I_d/I_b). For our *in vivo* arm data, we found a maximum I_d/I_b ratio of 0.15, which corresponds to an expected error of 1.2% in recovered signal based on numerical simulation results (Figure 5). To further validate these numerical results we tested our imaging system on a cylindrical phantom with imprinted letters (Figure 8 & 9) to compare the error in recovery. The calculated I_d/I_b ratios were 0.73 (black marker), 0.51 (red marker), and 0.39 (pencil). A maximum error of 40% was found for black permanent marker (highest ratio), which equates to the expected value from the numerical simulation results with the same ratio. We would like to point out, that the phantom experiments with blue paper were not aimed towards mimicking optical properties, rather than mimicking intensity ratios present when different structures with different optical properties are present in the area to be imaged. Due to this, we were able

to use paper and markers, which do not have comparable optical properties, but do have comparable intensity ratios. For interested readers, we suggest to use equations [22] and [23] for calculating I_d/I_b and for putting their work in the same context.

In vivo results demonstrated the importance of curvature correction on identifying underlying tissue structures in the intensity images (Figure 11) and consequently in the reconstructed blood volume and oxygenation maps (Figure 12). Whilst the accurate concentrations are unknown due to the lack of a control measurement, the curvature effect in the raw images causes distortions in reconstructed maps, leading to physiologically unreasonable over- and underestimation of chromophore concentration. After curvature correction, the chromophore concentrations are more uniform, except for areas of different physiology (veins). We demonstrated that the overall spatial distribution is improved over the uncorrected reconstruction results. Pixel wise comparison between areas was made possible.

CONCLUSION

We introduced a direct, robust, rapid and elegant methodology to correct for curvature artifacts present in many non-contact optical imaging modalities. The method is based on analysis of raw intensity images by one of two algorithms, either averaging or curve fitting, and does not require any additional measurements of the shape. As no additional data is required, an attractive feature of the method is that already acquired data can be curvature corrected and reanalyzed. The effectiveness of our technique was demonstrated on numerical simulations, phantom experiments and *in vivo* data acquired from forearms, using multi-spectral imaging. We evaluated both algorithms in the presence of noise, for different angles of sample orientation, for varying curvature, and for varying data signal, either varying in spatial frequency or contrast. Results showed that the curvature removal does not bias the recovered signal. They also demonstrated that the curve fitting approach is better for generalized geometries. However, care must be taken regarding degree of curvature, spatial frequency and data to background intensity ratios, if this approach is to be chosen over the averaging algorithm. Furthermore, results from phantom experiments showed that real intensity values can be recovered and objects with same optical properties but different shape can be directly and pixel wise compared. Based on the numerical simulation results, we found that in the case of *in vivo* arm data, a maximum error of less than 2% can be expected in the recovery of the signal. We demonstrated the curve fitting approach on *in vivo* data of the arm for intensity images as well as for reconstruction results of blood volume and oxygenation and showed the importance of taking the curvature into account if pixel wise assessment of skin chromophores is desired.

ACKNOWLEDGEMENTS

The research was funded by the Intramural Research Program of the Eunice Kennedy Shriver National Institute of Child Health and Human Development. The Graduate Partnership Program at the National Institutes of Health and the Department of Physics at the University of Vienna in Austria are also acknowledged.

Prepared by LLNL under Contract DE-AC52-07NA27344.

1. J. L. Kovar, M. A. Simpson, A. Schutz-Geschwender and D. M. Olive, "A systematic approach to the development of fluorescent contrast agents for optical imaging of mouse cancer models," Anal Biochem 367(1), 1-12 (2007)

2. K. Miyamoto, H. Takiwaki, G. G. Hillebrand and S. Arase, "Development of a digital imaging system for objective measurement of hyperpigmented spots on the face," Skin Res Technol 8(4), 227-235 (2002)

3. J. Pladellorens, A. Pinto, J. Segura, C. Cadevall, J. Anto, J. Pujol, M. Vilaseca and J. Coll, "A device for the color measurement and detection of spots on the skin," Skin Res Technol 14(1), 65-70 (2008)

4. B. Riordan, S. Sprigle and M. Linden, "Testing the validity of erythema detection algorithms," J Rehabil Res Dev 38(1), 13-22 (2001)

5. Y. Bae, J. S. Nelson and B. Jung, "Multimodal facial color imaging modality for objective analysis of skin lesions," Journal of biomedical optics 13(6), 064007 (2008)

6. S. G. Demos and R. R. Alfano, "Optical polarization imaging," Applied Optics 36(1), 150-155 (1997)

7. S. L. Jacques, J. R. Roman and K. Lee, "Imaging superficial tissues with polarized light," Lasers Surg Med 26(2), 119-129 (2000)

8. A. Sviridov, V. Chernomordik, M. Hassan, A. Russo, A. Eidsath, P. Smith and A. H. Gandjbakhche, "Intensity profiles of linearly polarized light backscattered from skin and tissue-like phantoms," Journal of biomedical optics 10(1), 14012 (2005)

9. A. P. Sviridov, V. Chernomordik, M. Hassan, A. C. Boccara, A. Russo, P. Smith and A. Gandjbakhche, "Enhancement of hidden structures of early skin fibrosis using

polarization degree patterns and Pearson correlation analysis," Journal of biomedical optics 10(5), 051706 (2005)

10. A. P. Sviridov, Z. Ulissi, V. Chernomordik, M. Hassan and A. H. Gandjbakhche, "Visualization of biological texture using correlation coefficient images," Journal of biomedical optics 11(6), 060504 (2006)

11. H. Arimoto, "Multispectral polarization imaging for observing blood oxygen saturation in skin tissue," Appl Spectrosc 60(4), 459-464 (2006)

12. H. Arimoto, "Estimation of water content distribution in the skin using dualband polarization imaging," Skin Res Technol 13(1), 49-54 (2007)

13. M. Attas, M. Hewko, J. Payette, T. Posthumus, M. Sowa and H. Mantsch, "Visualization of cutaneous hemoglobin oxygenation and skin hydration using near-infrared spectroscopic imaging," Skin Res Technol 7(4), 238-245 (2001)

14. D. J. Cuccia, F. Bevilacqua, A. J. Durkin and B. J. Tromberg, "Modulated imaging: quantitative analysis and tomography of turbid media in the spatial-frequency domain," Opt Lett 30(11), 1354-1356 (2005)

15. A. Vogel, V. V. Chernomordik, J. D. Riley, M. Hassan, F. Amyot, B. Dasgeb, S. G. Demos, R. Pursley, R. F. Little, R. Yarchoan, Y. Tao and A. H. Gandjbakhche, "Using noninvasive multispectral imaging to quantitatively assess tissue vasculature," Journal of biomedical optics 12(5), 051604 (2007)

16. A. Vogel, B. Dasgeb, M. Hassan, F. Amyot, V. Chernomordik, Y. Tao, S. G. Demos, K. Wyvill, K. Aleman, R. Little, R. Yarchoan and A. H. Gandjbakhche, "Using quantitative imaging techniques to assess vascularity in AIDS-related Kaposi's sarcoma," Conf Proc IEEE Eng Med Biol Soc 1(232-235 (2006)

17. M. Westhauser, G. Bischoff, Z. Borocz, J. Kleinheinz, G. von Bally and D. Dirksen, "Optimizing color reproduction of a topometric measurement system for medical applications," Med Eng Phys 30(8), 1065-1070 (2008)

18. V. Paquit, J. R. Price, F. Meì□riaudeau, K. W. Tobin and T. L. Ferrell, "Combining near-infrared illuminants to optimize venous imaging," in Progress in Biomedical Optics and Imaging - Proceedings of SPIE (2007).

19. V. Paquit, J. R. Price, R. Seulin, F. Meì□riaudeau, R. H. Farahi, K. W. Tobin and T. L. Ferrell, "Near-infrared imaging and structured light ranging for automatic catheter insertion," in Progress in Biomedical Optics and Imaging - Proceedings of SPIE (2006).

20. S. Gioux, A. Mazhar, D. J. Cuccia, A. J. Durkin, B. J. Tromberg and J. V. Frangioni, "Three-dimensional surface profile intensity correction for spatially modulated imaging," Journal of biomedical optics 14(3), 034045 (2009)

21. D. J. Cuccia, F. Bevilacqua, A. J. Durkin, F. R. Ayers and B. J. Tromberg, "Quantitation and mapping of tissue optical properties using modulated imaging," Journal of biomedical optics 14(2), 024012 (2009)

22. H. D. Zeman, G. Lovhoiden, C. Vrancken and R. K. Danish, "Prototype vein contrast enhancer," Optical Engineering 44(8), (2005)

23. S. L. Jacques, "Skin Optics," Oregon Medical Laser Center News <http://omlc.ogi.edu/news/jan98/skinoptics.html>((1998)

24. I. V. Meglinski and S. J. Matcher, "Quantitative assessment of skin layers absorption and skin reflectance spectra simulation in the visible and near-infrared spectral regions," Physiol Meas 23(4), 741-753 (2002)

25. S. Prahl, "Skin Optics," Oregon Medical Laser Center News <http://omlc.ogi.edu/spectra/hemoglobin/index.html>((1998)

26. A. H. Gandjbakhche and G. H. Weiss, "Random walk and diffusion-like models of photon migration in turbid media," Progress in Optics XXXIV(V), 335-402 (1995)

FIGURE LEGENDS

Figure 1 Examples of multi-spectral intensity images containing the curvature effect are shown. (a) Shows an intensity image of a healthy volunteer's lower arm, (b) an intensity image of the cylindrical phantom and (c) the flat phantom. Images shown were taken at a wavelength of 800nm.

Figure 2 (a) Data wave (a sine grating), superimposed on (b – i) a cylindrical object without noise and (b – ii) with 50% noise. Three different approaches for curvature removal were tested, (c) exact kernel deconvolution, (d) horizontal and vertical averaging and (e) curve fitting. Qualitatively all three approaches perform equally well in the noise free scenario (i), as well as in the noise scenario (ii). The point-wise percentage error for the noise case is shown in column (iii).

Figure 3 (a) Error in reconstruction caused by rotation of object from image axis. The cylindrical object was rotated 90 degrees, in 5 degree steps. The average error in reconstruction is plotted against the angle of rotation for all three methods. The averaging method highly depends on the orientation of the objects axis to the image axis, whereas the curve fitting method does not. (b) Error due to varying curvature. Changes in the radius, therefore maximum angle of the cylinder were evaluated. The error displayed has units of the data signal, which is of the order of 0.01. The curve fitting method shows an error greater than the data for angles between 85 and 35 degree and brakes down at angles > 85 degree. At angles smaller than 35 degrees, the error is smaller than the data signal. The averaging method is not affected by the angle.

Figure 4 (a) Gradual degradation of the curvature correction using the curve fitting approach, when data with decreasing spatial frequencies (top to bottom) are applied. The left column shows the data waves and right column the deconvolved ones. (b) Error in reconstruction caused by low spatial frequencies in data. The dependence of spatial frequency of the data wave for the curve fitting approach is pointed out by plotting the average error in reconstruction against the number of cycles of the sine grating in the data wave. As expected, the averaging approach is not affected by the varying spatial frequency.

Figure 5 Error in reconstruction caused by increasing data to background signal level. The percentage error in reconstruction was plotted against the ratio of data to background (I_d/I_b) for all three methods. (a) shows the percentage error for ratios up to 1 (data equals background) and (b) shows the same graph, but zoomed in to physiologically reasonable ratios. The error increases dramatically as the ratio goes to 1.

Figure 6 (a) Dependence of polynomial order on the fitting quality. The averaged, normalized cross-section through the cylinder (along y-axis) is plotted for each polynomial order tested. Order five and six fit the object shape accurately leaving only minor residuals (<2%) at the edges of the cylinder. (b) Shows the dependence of polynomial order on normalized standard deviation of the curvature corrected cylinder, illustrated by the L-curves.

Figure 7 The curvature correction based on curve fitting on the cylindrical phantom without data content and compared to the flat phantom. (a) Shows the curvature uncorrected intensity image, (b) the curvature corrected intensity image, and (c) shows the flat phantom. (d) shows the averaged cross section of (a-c) with errorbars given by the standard deviation over all rows.

Figure 8 The curvature correction based on curve fitting on the cylindrical phantom with data (letters). Intensity images are shown before (i and iii) and after (ii and iv) curvature correction. Different contrast agents were used, with decreasing data to background ratios. The different I_d/I_b ratios are (a) 0.73, (b) 0.51 and (c) 0.39. The figure qualitatively shows the dependence of data to background ratio on the correction performance.

Figure 9 Dependence of contrast on the curvature correction. The I_d/I_b ratio is plotted against the normalized standard deviation of the background of the curvature corrected image at the wavelength of 800nm. Both cases of feature alignment are shown, as well as in comparison to the flat phantom without contrast agents.

Figure 10 The effect of multiple iterations on the goodness of fit of curvature is shown in this graph. (a) Shows a cross-section through the curvature fit is shown for all six iterations. Black arrows indicate the location of veins. It can be seen that the effect of veins disappear after several iterations, leaving a smooth curvature. The L-curve (b) shows the squared error against number of iterations.

Figure 11 Curvature correction for *in vivo* data. Intensity images of a healthy volunteer's arm (a) before and (b) after correction are demonstrated for all six wavelengths. The qualitative enhancement in image quality can be seen in the corrected images.

Figure 12 The effect of curvature correction on quantification of fraction blood oxygenation (a, c) and fraction blood volume (b, d). Reconstruction results before curvature correction (a, b) are clearly biased by it. Results after correction (c, d) don't show this effect, which can be seen in more detail in the cross sectional plots shown in (e, f – uncorrected in blue, corrected in green). The cross sections shown are indicated by the dotted line in (a). Detailed assessment of tissue chromophore concentration was made possible.

FIGURES

Figure 1

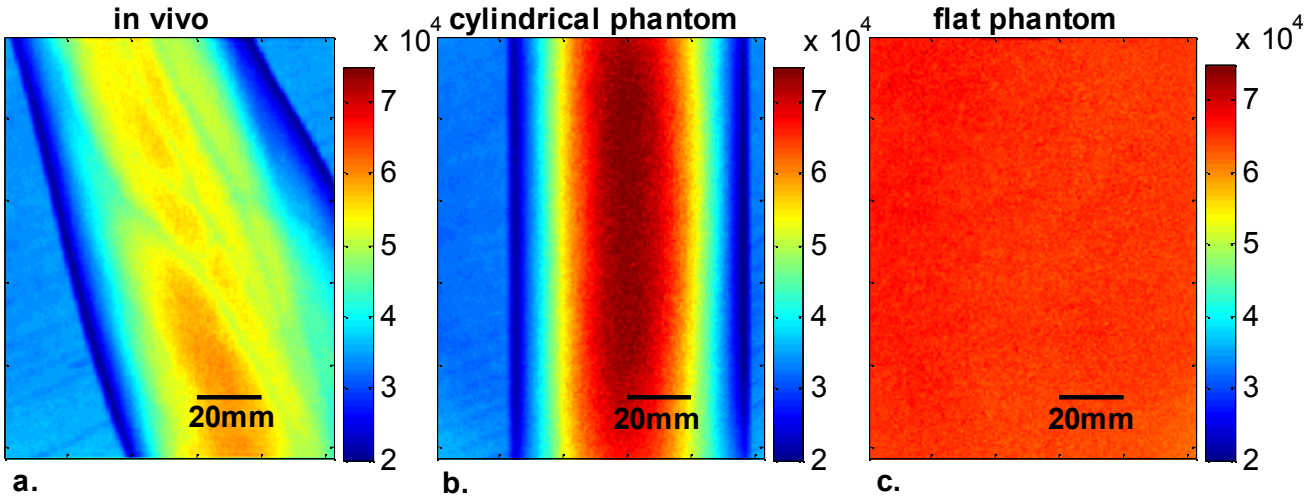

Figure 2

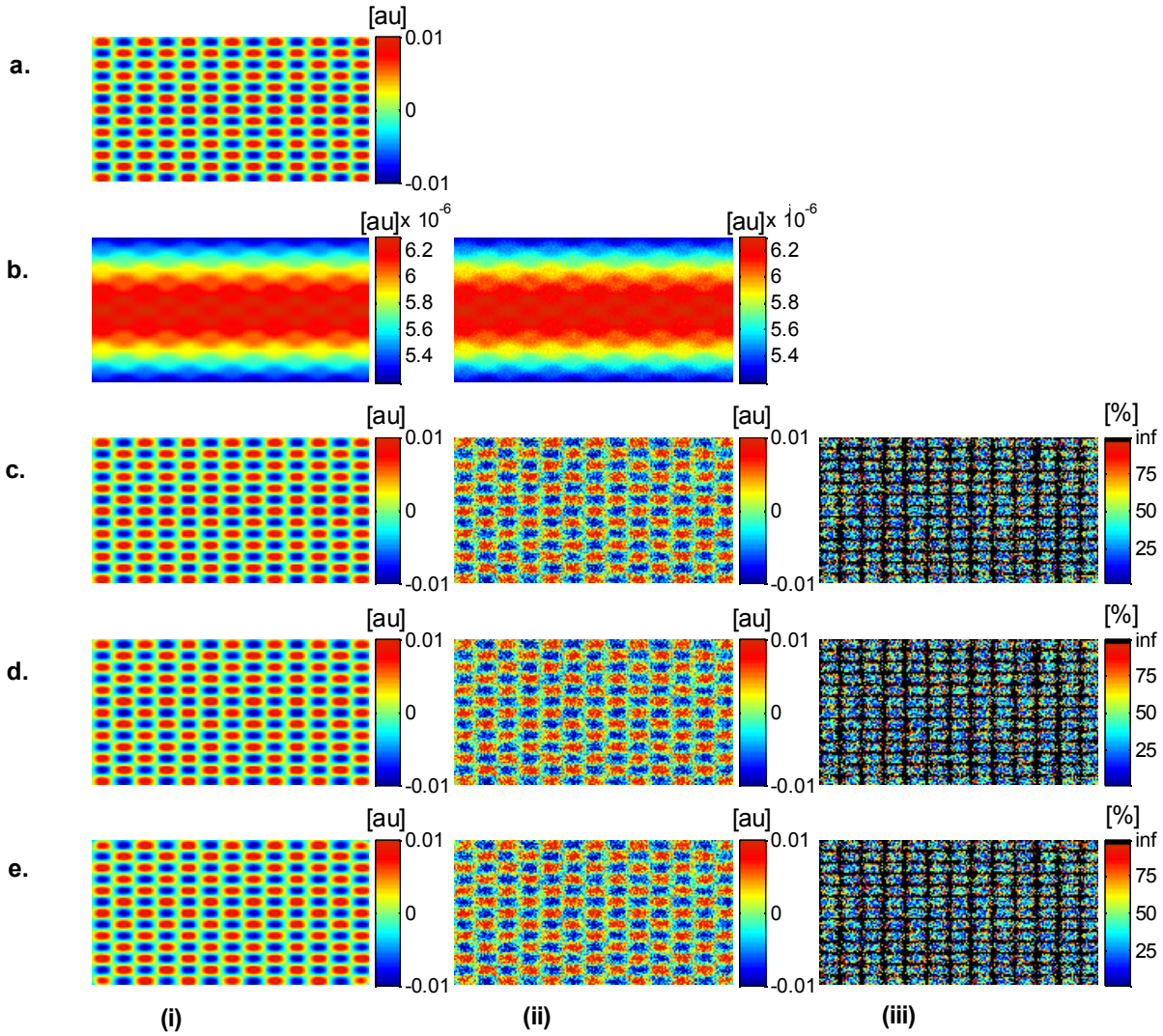
a.
[au]
0.01
0
-0.01
b.
[au]x 10^-6
6.2
6
5.8
5.6
5.4
[au]x 10^-6
6.2
6
5.8
5.6
5.4
c.
[au]
0.01
0
-0.01
[au]
0.01
0
-0.01
[%]
inf
75
50
25
d.
[au]
0.01
0
-0.01
[au]
0.01
0
-0.01
[%]
inf
75
50
25
e.
[au]
0.01
0
-0.01
[au]
0.01
0
-0.01
[%]
inf
75
50
25
(i)
(ii)
(iii)

Figure 3

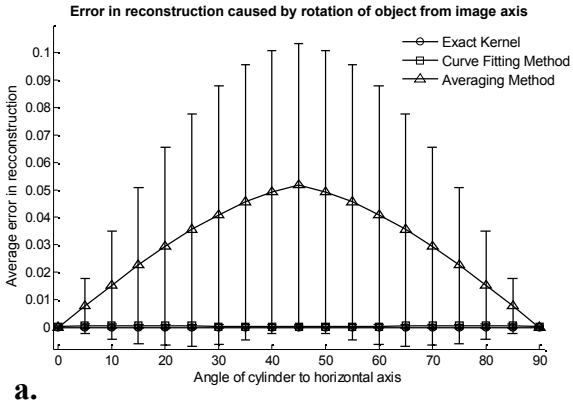
Error in reconstruction caused by rotation of object from image axis
Exact Kernel
Curve Fitting Method
Averaging Method
Average error in reconstruction
0.1
0.09
0.08
0.07
0.06
0.05
0.04
0.03
0.02
0.01
0
0 10 20 30 40 50 60 70 80 90
Angle of cylinder to horizontal axis

a.

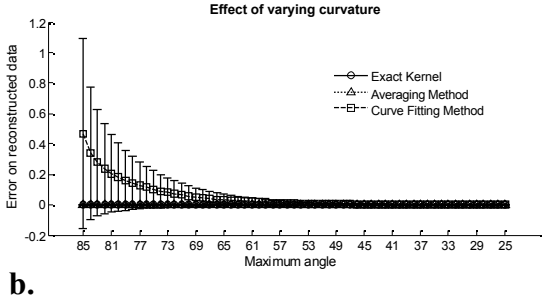
Effect of varying curvature
Exact Kernel
Averaging Method
Curve Fitting Method
Error on reconstructed data
1.2
1
0.8
0.6
0.4
0.2
0
-0.2
85 81 77 73 69 65 61 57 53 49 45 41 37 33 29 25
Maximum angle

b.

Figure 4

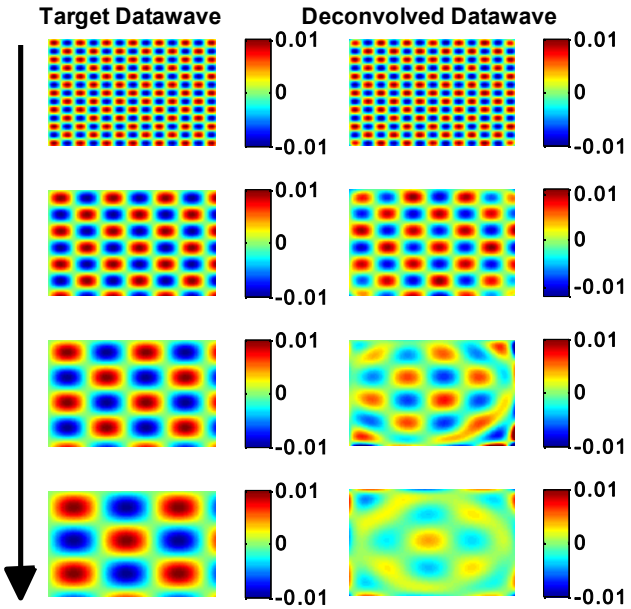
Target Datawave
Deconvolved Datawave
0.01
0
-0.01

a.

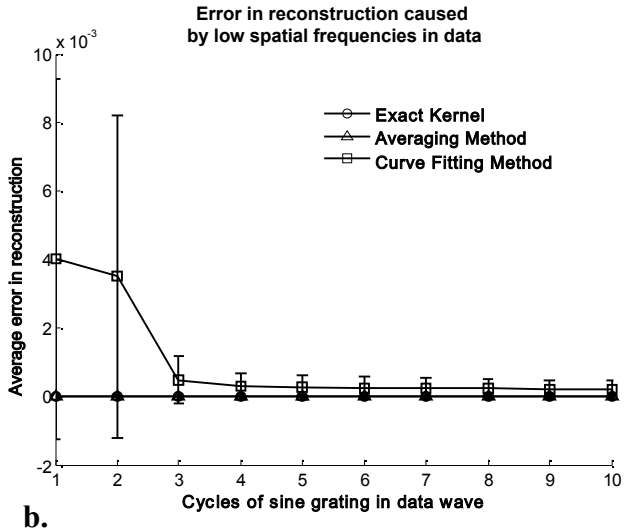
Error in reconstruction caused
by low spatial frequencies in data
x 10^-3
10
8
6
4
2
0
-2
Average error in reconstruction
Exact Kernel
Averaging Method
Curve Fitting Method
1
2
3
4
5
6
7
8
9
10
Cycles of sine grating in data wave

b.

Figure 5

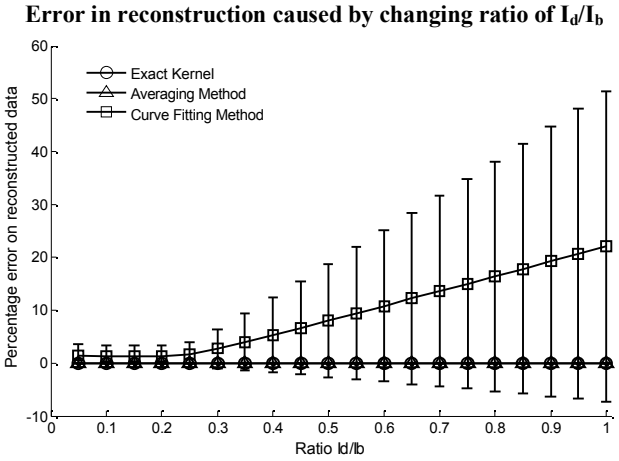
Error in reconstruction caused by changing ratio of I_d/I_b
Exact Kernel
Averaging Method
Curve Fitting Method
Percentage error on reconstructed data
Ratio Id/Ib
60
50
40
30
20
10
0
-10
0
0.1
0.2
0.3
0.4
0.5
0.6
0.7
0.8
0.9
1

Figure 6

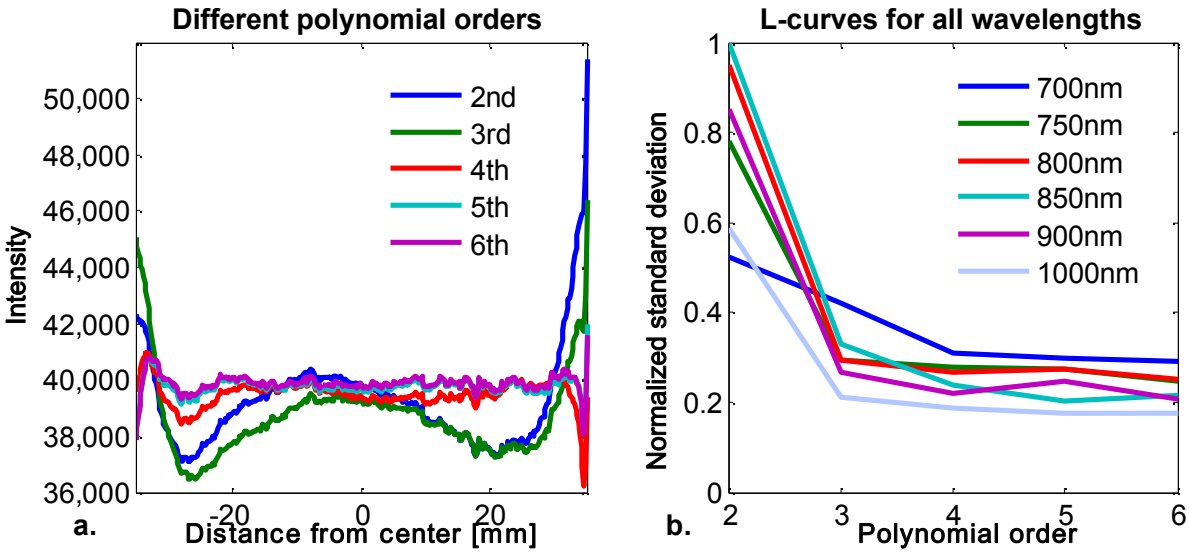
Different polynomial orders
Intensity
50,000
48,000
46,000
44,000
42,000
40,000
38,000
36,000
-20
0
20
Distance from center [mm]
2nd
3rd
4th
5th
6th
a.
L-curves for all wavelengths
Normalized standard deviation
1
0.8
0.6
0.4
0.2
0
2
3
4
5
6
Polynomial order
700nm
750nm
800nm
850nm
900nm
1000nm
b.

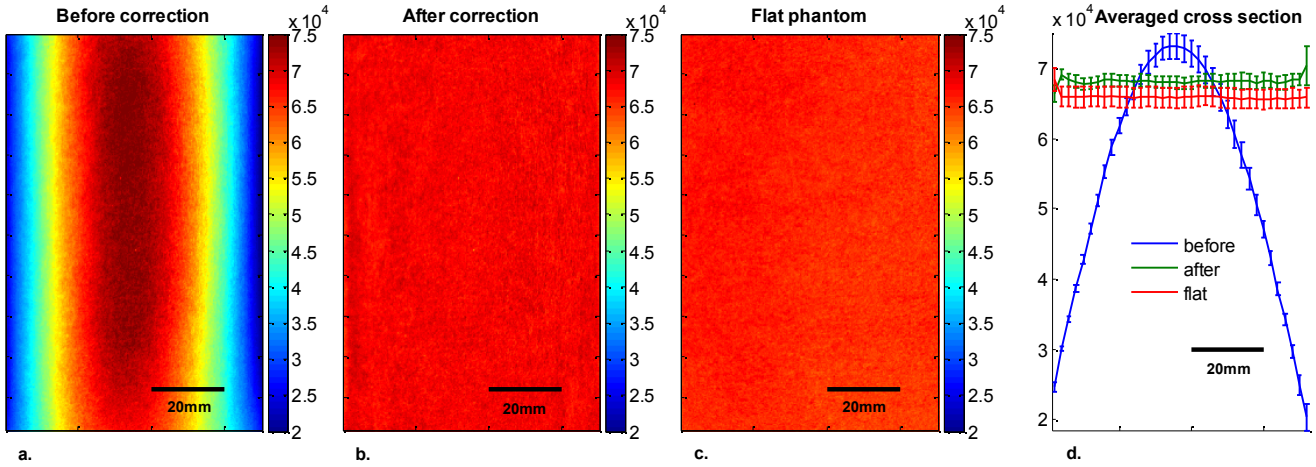
Before correction
x 10^4
7.5
7
6.5
6
5.5
5
4.5
4
3.5
3
2.5
2
20mm
a.
After correction
x 10^4
7.5
7
6.5
6
5.5
5
4.5
4
3.5
3
2.5
2
20mm
b.
Flat phantom
x 10^4
7.5
7
6.5
6
5.5
5
4.5
4
3.5
3
2.5
2
20mm
c.
x 10^4
Averaged cross section
7
6
5
4
3
2
before
after
flat
20mm
d.

Figure 7

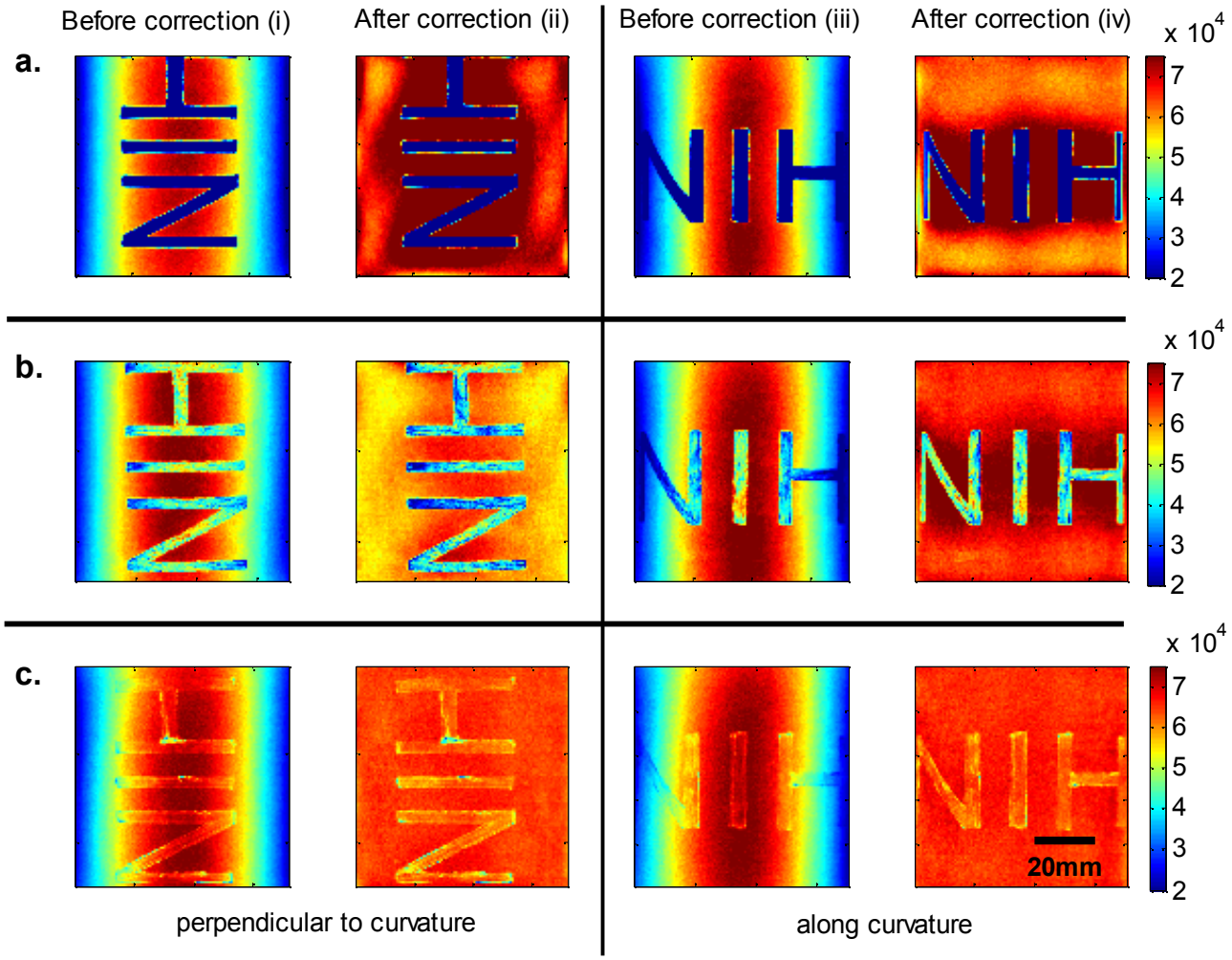
Before correction (i)
After correction (ii)
Before correction (iii)
After correction (iv)
a.
b.
c.
x 10^4
7
6
5
4
3
2
20mm
perpendicular to curvature
along curvature

Figure 8

Figure 9

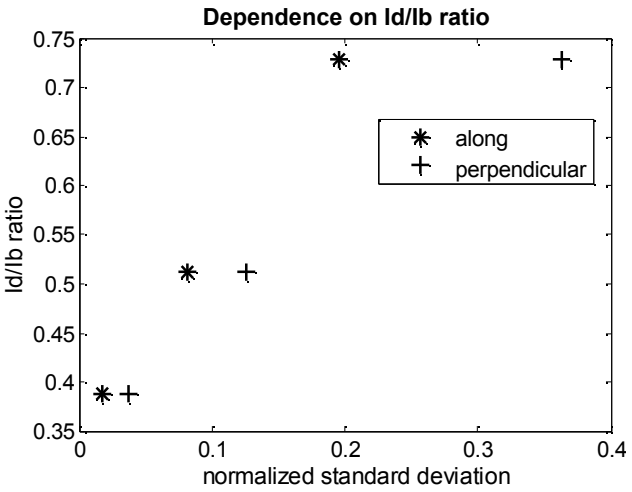
Dependence on ld/lb ratio
ld/lb ratio
normalized standard deviation
along
perpendicular
0.75
0.7
0.65
0.6
0.55
0.5
0.45
0.4
0.35
0
0.1
0.2
0.3
0.4

Figure 10

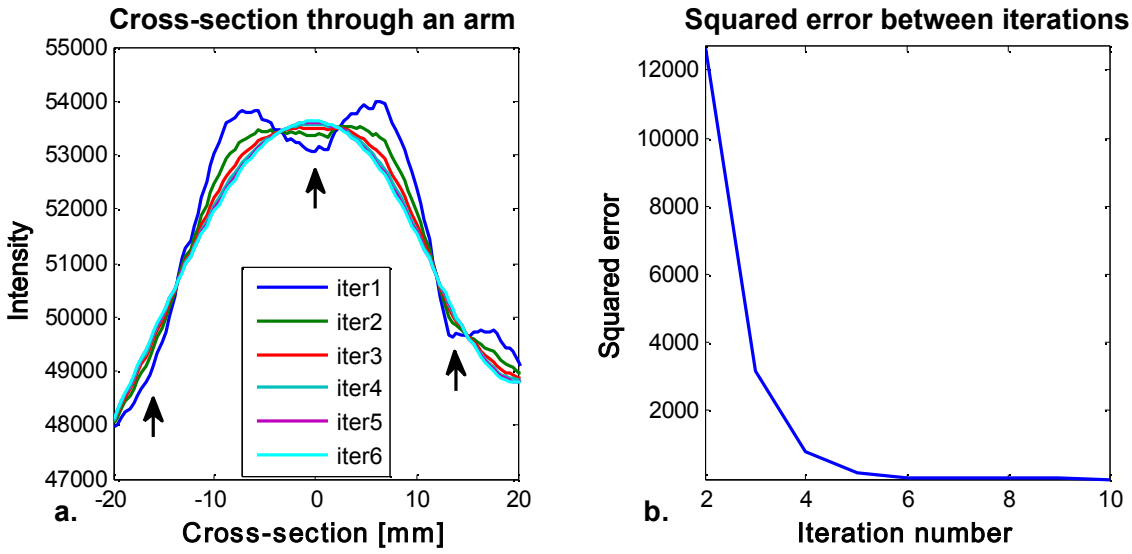
Cross-section through an arm
Intensity
Cross-section [mm]
iter1
iter2
iter3
iter4
iter5
iter6
a.
Squared error between iterations
Squared error
Iteration number
b.

Figure 11

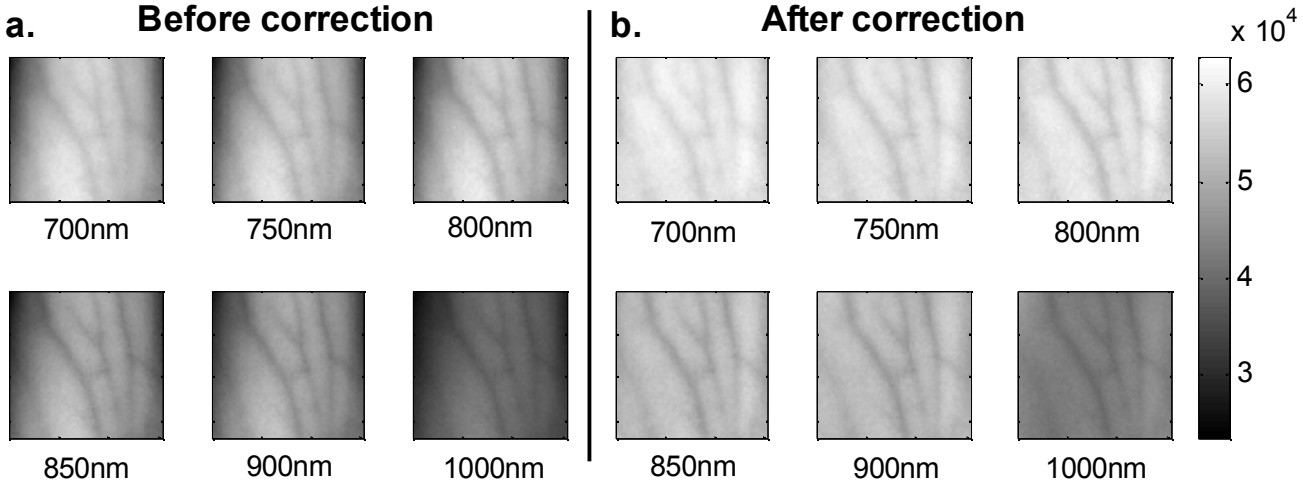
a.
Before correction
b.
After correction
x 10^4
6
5
4
3
700nm
750nm
800nm
850nm
900nm
1000nm
700nm
750nm
800nm
850nm
900nm
1000nm

Figure 12

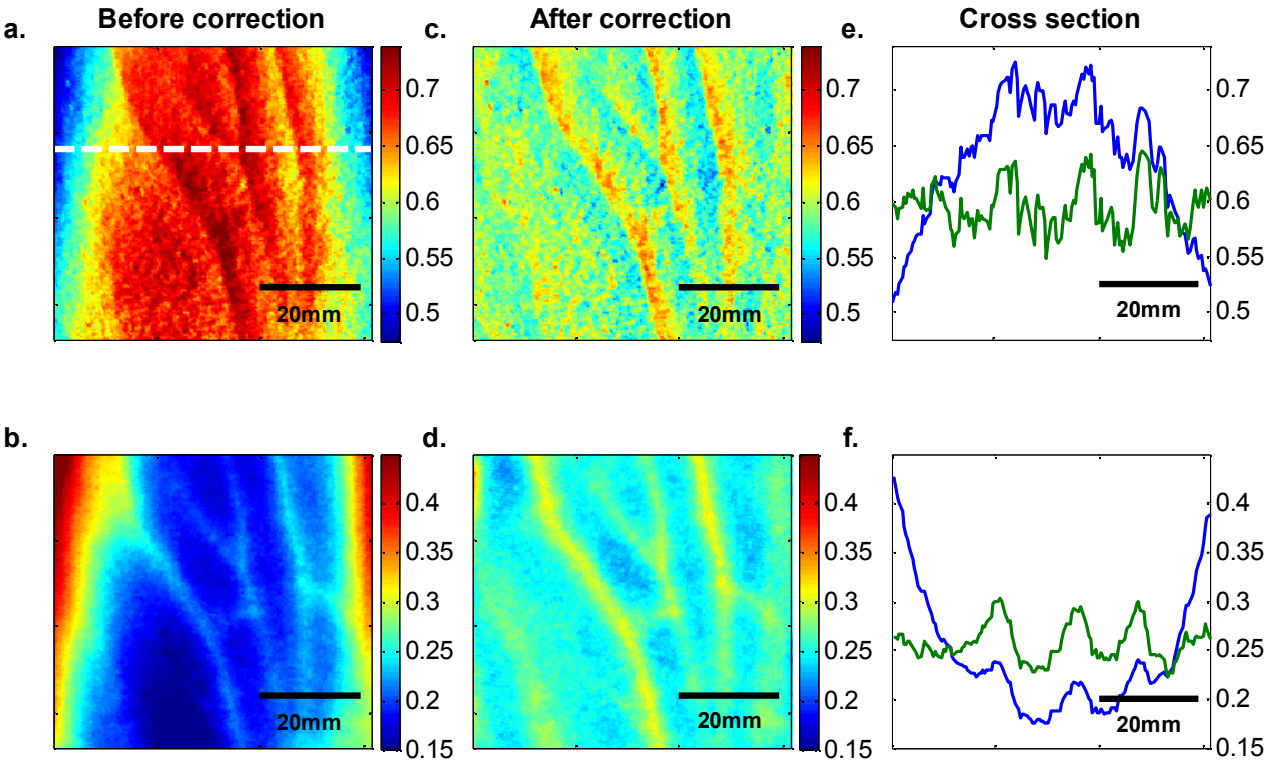
a.
Before correction
c.
After correction
e.
Cross section
b.
d.
f.
20mm
0.7
0.65
0.6
0.55
0.5
0.4
0.35
0.3
0.25
0.2
0.15

Table 1: Optical properties of the skin.

Wavelength (nm)	$\mu_{deoxy}\ [mm^{-1}]$	$\mu_{oxy}\ [mm^{-1}]$	$v_m * \mu_{mel}\ [mm^{-1}]$	$\mu_s\ [mm^{-1}]$
700	1.068	0.232	1.772	1.912
750	0.788	0.330	1.408	1.606
800	0.478	0.468	1.136	1.372
850	0.424	0.583	0.928	1.190